# ANNALS OF THE NEW YORK ACADEMY OF SCIENCES

# Sympathetic innervation of the interscapular brown adipose tissue in mouse

Marie François,[a] Hayden Torres,[a] Clara Huesing,[a] Rui Zhang, Carson Saurage, Nathan Lee, Emily Qualls-Creekmore, Sangho Yu, Christopher D. Morrison, David Burk, Hans Rudolf Berthoud, and Heike Münzberg

Neurobiology of Nutrition and Metabolism Department, Pennington Biomedical Research Center, Louisiana State University System, Baton Rouge, Louisiana

Address for correspondence: Heike Münzberg, Neurobiology of Nutrition and Metabolism Department, Pennington Biomedical Research Center, Louisiana State University System, 6400 Perkins Rd, Baton Rouge, LA 70808. Heike.Munzberg@pbrc.edu

**The recent discovery of significant brown fat depots in adult humans has revived discussion of exploiting brown fat thermogenesis in the control of energy balance and body weight. The sympathetic nervous system (SNS) has a key role in the activation of brown fat and functional mapping of its components will be crucial for the development of specific neuromodulation techniques. The mouse is an important species used for molecular genetic modulations, but its small size is not ideal for anatomical dissections, thus brown fat innervation studies are mostly available in larger rodents such as rats and hamsters. Here, we use pseudorabies virus retrograde tracing, whole tissue clearing, and confocal/light sheet microscopy to show the location of pre- and postganglionic neurons selectively innervating the interscapular brown adipose tissue (iBAT) in the mouse. Using iDISCO whole tissue clearing, we identified iBAT projecting postganglionic neurons in the caudal parts of the ipsilateral fused stellate/T1, as well as the T2−T5 sympathetic chain ganglia and preganglionic neurons between levels T2 and T6 of the ipsilateral spinal cord. The methodology enabled high-resolution imaging and 3D rendering of the specific SNS innervation of iBAT and will be helpful to discern peripheral nervous system innervation of other organs and tissues.**

**Keywords:** sympathetic chain ganglia; transsynaptic retrograde tracing; iDISCO; tissue clearing; imaging; pseudorabies virus

## Introduction

Interest in brown adipose tissue (BAT) as a site for burning off excess calories in the fight against obesity flared up 35 years ago[1,2] and returned recently after a long hiatus.[3,4] While it has been clear that brown fat thermogenesis is important for the maintenance of body temperature for most homeothermic animals and human infants, a significant contribution in adult humans has only recently been suggested by the rediscovery of significant BAT depots[1,4–8] (for recent reviews, see Refs. 9 and 10). Besides responsiveness to photoperiod and ambient temperature,[11–13] BAT activity in adult humans increases after a high-calorie meal.[14] This latter finding revives Rothwell and Stock's original idea of "Luxuskonsumption," or the ability of BAT to burn off extra calories and prevent obesity.[15]

In rodents, interscapular BAT (iBAT) is the largest depot, with smaller depots in the mediastinum, along the cervical and thoracic aorta, and around the kidneys.[16] In humans, BAT is less centralized than in rodents, with significant depots in supraclavicular, neck, and paraspinal regions.[4,17,18] Based on numerous experiments with denervation of the interscapular pads in rodents, as well as pharmacological studies using β3-adrenergic agonists and blockers, the main driver of BAT thermogenesis seems to be its noradrenergic sympathetic innervation.[19–27] Furthermore, a recent

---

[a]Co-first authors.

study demonstrating increased thermogenesis by electrical field stimulation of the dorsal surface of iBAT in rats[28] suggests that stimulation of noradrenaline release from sympathetic nerve terminals is required for this effect. The functional necessity of the sympathetic nervous system (SNS) for intact BAT function is demonstrated by surgical and chemical denervation methods, which block or greatly reduce most cold-induced BAT adaptations like UCP1 induction, increased blood flow, higher mitochondrial density, enhanced glucose uptake, and activation of thyroid-activating enzymes.[29]

Thus, there is an increasing need to visualize the sympathetic innervation of BAT efficiently to make this tissue accessible for peripheral nerve stimulation, verification of viral labeling extent, and specialized pharmacotherapy. Here, we identify different reporter mice that efficiently visualize peripheral sympathetic innervation and establish the use of immunohistochemical double labeling and tissue clearing for large thoracic specimens to identify the location and distribution of postganglionic sympathetic neurons innervating iBAT in the mouse using the widely utilized pseudorabies virus (PRV).

## Materials and methods

### Animals

Transgenic tgDbh-Cre mice (stock #: 032081-UCD, Tg(Dbh-Cre)KH212Gsat/Mmucd, Mutant Mouse Resource and Research Center, breeding pairs were obtained from Dr. Derbenev, Tulane University), TH-IRES-Cre mice (EM: 00254; B6.129×1-Th$^{tm1(Cre)Te}$/Kieg; European Mouse Mutant Archive; breeding pairs were obtained from Dr. Louis de Lecea, Stanford University) crossed with Rosa-Tomato$^{fl/fl}$ mice (stock #: 007914; B6.Cg-Gt(ROSA) 26Sor$^{tm14(CAG-tdTomato)Hze}$/J, Jackson Laboratories) to generate TH:Tomato reporter mice. Both male and female offspring were group-housed at a 12 h:12 h light/dark cycle with *ad lib* access to food and water unless stated otherwise. Animal genotypes were confirmed by PCR from tail biopsies DNA (tgDbh-Cre mice: transgene forward 5′-AATGGCAGAGTGGGGGTTGGG-3′; transgene reverse 5′-CGGCAAACGGACAGAAGCATT-3′; TH-IRES-Cre: Cre reverse 5′-GAT-ACC-TGG-CCT-GGT-CTG-3′; wild-type/Cre forward 5′-CAC-CCT-GAC-CCA-AGC-ACT-3′; wild-type reverse 5′-CTT-TCC-TTC-CTT-TAT-TGA-GAT-

3′; Rosa-Tomato$^{fl/fl}$ mice: wild-type forward 5′-AAG GGA GCT GCA GTG GAG TA-3′; wild-type reverse 5′-CCG AAA ATC TGT GGG AAG TC-3′; mutant reverse 5′-GGC ATT AAA GCA GCG TAT CC-3′; mutant forward 5′-CTG TTC CTG TAC GGC ATG G-3′). The Institutional Animal Care and Use Committee approved all animal experiments.

### PRV infection of the iBAT

In Figure 1A, the experimental steps are summarized schematically. The iBAT ($n = 9$ mice; 7 F, 2 M) received a unilateral injection with green fluorescent protein (GFP) expressing PRV (PRV-GFP, viral titer, $1 \times 10^9$ pfu/mL, Lot #2007, $5 \times 100$ nL, kindly provided by the National Center for Experimental Neuroanatomy with Neurotropic Viruses, Pittsburgh, PA). Mice were anesthetized with isoflurane/oxygen and iBAT was exposed by an intrascapular incision. The virus was then injected with a pulled glass pipette (tip diameter $\sim 5\,\mu$m) attached to a 0.5-$\mu$L Hamilton$^{®}$ syringe. Five separate injections of 100 nL were distributed over the right iBAT depot, holding the pipette in place for 10 s to prevent backflow. Injection sites were then dried with gauze to prevent leakage to surrounding tissue and the circulation. Mice were single housed post viral infection for 72 and 96 h, and then perfused and processed as described below. Controls included dripping the same total amount of PRV (500 nL) onto the surface of the iBAT depot ($n = 2$) or surgical ($n = 2$) denervation of iBAT.

### Perfusion and fluorescence-guided dissection of relevant tissue blocks

Mice injected with PRV were perfused at 3−4 days post viral infection. Perfusion and immunohistochemistry were performed as previously described.[30] Briefly, mice were deeply anesthetized with isoflurane and transcardially perfused with ice-cold physiological saline followed by 10% buffered formalin.

Thoracic organs were removed and successful infection was verified with a fluorescent stereomicroscope (Nikon, SMZ25, Melville, NY) and only animals with visible sympathetic chain ganglia infection were further included in tissue dissection and analysis. The BAT was removed and the entire spinal cord was further cleared of excessive muscle mass. A laminectomy was performed to allow imaging of preganglionic intermediolateral (IML)
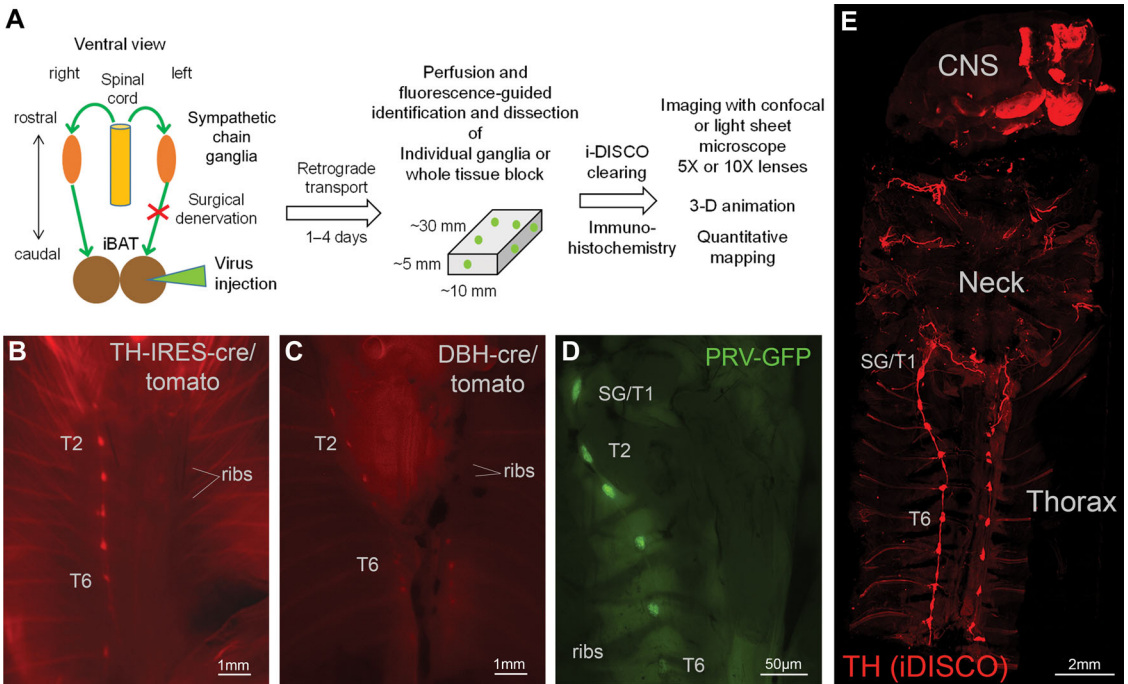
**Figure 1.** Overview of experimental design, dissection technique, and whole body tissue clearing. (A) Flow diagram of experimental design. (B and C) Ventral views of eviscerated, perfused TH:Tomato mouse (B), Dbh:Tomato mouse (C) using stereomicroscope. (D) Ventral view of eviscerated, perfused wild-type mouse 96 h post-PRV-GFP injection into the right iBAT pad using stereomicroscope. Note labeling of right, but not left sympathetic chain ganglia. (E) Confocal microscope image of the whole upper body of a mouse after iDISCO immunohistochemistry with TH and tissue clearing. Note labeling of the bilateral sympathetic chain, neck nerves, and brain areas. TH, tyrosine hydroxylase; DBH, dopamine beta-hydroxylase; PRV, pseudorabies virus; GFP, green fluorescent protein; SG, stellate ganglion; T1—T7, ganglia for thoracic levels 1—7.

neurons. The spinal cord was cut at the thoracic level T7/T8 to accommodate optimal imaging capacities. The tissue was postfixed in formalin overnight and transferred to PBS-azide (2% sodium azide in PBS). All PRV-GFP–infected tissue was dehydrated in methanol (20%, 40%, 60%, 80%, and 100%, 1 h each) and stored in 100% methanol until further processing for staining and clearing as described below.

*Immunohistochemistry and tissue clearing*
Immunohistochemical staining was performed following the iDISCO method from Renier *et al.* (https://idisco.info/idisco-protocol/update-history/) with modifications. Briefly, after methanol dehydration, tissues were treated with 5% $H_2O_2$ in methanol (MeOH) overnight at 4 °C (1 volume 30% $H_2O_2$/5 volumes methanol, ice-cold), followed by washes in 100% methanol for 1 h and rehydrated in a series of MeOH /PBS (80%, 60%, 40%, and 20%)

for 1 h each. Samples were further incubated in 1 x PBS/0.2% Triton X-100 twice (PTx.2 solution) for 1 h each and permeabilized in 400 mL PTx.2, 11.5 g glycine, 100 mL DMSO at 37 °C with shaking for 2 days. See Table S1 (online only) for a complete list of antibodies used. After that, tissues were blocked in 42 mL PTx.2, 3 mL donkey serum (Jackson ImmunoResearch, West Grove, PA), and 5 mL DMSO over 2.5 days at 37 °C with shaking. Then, tissues were incubated with primary antibodies (chicken anti-GFP [1:400], Abcam, Cambridge, MA; rabbit anti-TH [1:400], Millipore, Burlington, MA) in PBS with 20% Tween 20 and 10 mg/mL heparin (PTwH)/5% DMSO/3% donkey serum at 37 °C with shaking for at least 7 days. Following primary staining, tissue samples were washed in PtWH 4—5 times in 60-min increments and then incubated in PtwH overnight. Samples were then subjected to secondary staining in PTwH/3% donkey serum for 1.5 weeks. Following primary

staining, tissue samples were washed in PtwH 4—5 times 1 h or until the following day.

Samples were dehydrated in MeOH/H$_2$O series, incubated in 66% dichloromethane (DCM, Sigma-Aldrich, St. Louis, MO)/33% MeOH at room temperature, and then in 100% DCM for 15 min twice with agitating on a rocker to rinse out any remaining MeOH. Tissues were stored in dibenzyl ether (DBE, Sigma-Aldrich) until imaging.

*Microscopy and image processing*
Spine sample imaging utilizing both a Leica SP5 confocal microscope (Leica Biosystems Inc., Buffalo Grove, IL) and a LaVision light sheet microscope (LaVision BioTec, Bielefeld, Germany). Specimen imaging in the organic solvent required immersion of the microscope objective in it, which is a capability of the light sheet but not the confocal microscope. Therefore, we used a handcrafted chamber for the confocal microscope to allow safe specimen access without damaging the equipment. Overview 3D image stacks were generated for the spine with a dorsal view to reveal PRV labeling in the IML column. 3D image stacks with a ventral view revealed thoracic and lumbar sympathetic chain ganglia and the celiac ganglion. Images of tyrosine hydroxylase (TH) and PRV labeling were collected for all samples. Higher magnification images were generated (10×) for PRV-positive sympathetic chain ganglia and the corresponding dorsal root ganglia (DRG), as indicated in figures, as well as for PRV-positive IML neurons. Note, even though confocal and light sheet microscopy both have advantages and disadvantages, at this level of analysis we used both systems interchangeable and both systems were sufficient to obtain single-cell resolution of PRV-labeled postganglionic neurons.

*Quantitative analyses of postganglionic neurons*
Among all investigated animals with successful PRV labeling, no evidence was found for pre- or postganglionic PRV labeling beyond thoracic level T8 and T7, respectively. Thus, we performed the systematic analysis only for the rostral portion of the spinal cord (the stellate ganglion to the sympathetic chain ganglion T8).

Overview images (5× magnification/1.0 zoom factor) showing the ventral (sympathetic chain ganglia) and dorsal (IML) view of the spinal cord were aligned to determine the thoracic levels of sympathetic chain ganglia and IML PRV labeling. We further investigated 10× magnification images to analyze PRV-labeled portions in more detail. Individual sympathetic chain ganglia were further quantified for the number of PRV-labeled neurons as a measure of infection efficiency and consistency for individual cases. 3D images included DRG for each sympathetic chain ganglia level and allowed evaluation for PRV labeling of sensory cell bodies. Within sympathetic chain ganglia, we estimated cell counts for PRV-positive neurons in z-stack images manually with the Adobe® Photoshop® count tool (Adobe Photoshop CS6, San Jose, CA), and an automated 3D analysis of cell counts utilizing the Imaris 9.2 spot counting feature (Bitplane AG, Concord, MA).

## Results

*Whole body* in situ *imaging and dissection of SNS components using TH:Tomato reporter mice*
In order to guide the dissection of the thoracic specimen that would retain components of the SNS, we wanted to capitalize on the powerful ability of reporter gene expression. Most reporter lines are well characterized for their expression profile in the central nervous system, while reporter expression in peripheral nerves remains unexplored. We found that knock-in TH:Tomato mice and transgenic Dbh:Tomato mice both showed strong fluorescence in noradrenergic nerves. After formalin fixation and removing the viscera, the bilateral sympathetic chain ganglia could be identified using a fluorescent stereomicroscope with a long working distance (Fig. 1). Knock-in TH:Tomato mice (Fig. 1B) showed stronger fluorescence compared to transgenic Dbh:Tomato mice (Fig. 1C), but both mouse lines showed bright fluorescence, revealing sympathetic chain ganglia and interconnecting nerve strands even at lower magnification. In contrast, our initial attempts using transgenic TH:Tomato mice (B6.Cg-*7630403G23Rik*$^{Tg(Th-cre)1Tmd}$/J, Stock# 008601) showed only sporadic fluorescent signal with only one or two Tomato-positive cells per thoracic sympathetic ganglia (data not shown). Thus, in our hands, knock-in TH:Tomato mice and transgenic Dbh:Tomato mice were most useful to visualize sympathetic chain ganglia, and associated nerves, and to clean ganglia of obscuring tissues (e.g., ganglia adipose tissue). Sympathetic

chain ganglia can be visualized without reporter gene expression, but the celiac/mesenteric ganglia complex is not visible without fluorescent labeling and abdominal chain ganglia are easily confused regarding to their thoracic and lumbar levels without fluorescent guidance specifically for the untrained experimenter.

### Clearing of large tissue blocks reveals 3D anatomy of sympathetic chain and other components of the SNS

Earlier work in embryos or newborn mice has used whole body clearing techniques to visualize sympathetic chain ganglia; however, this technique has not been adapted to substantially larger adult mice with excessive muscle and adipose tissue mass. However, recent histological advances have promoted tissue clearance for a larger specimen like the brain and human embryos,[31] suggesting that these techniques might also be suitable to visualize sympathetic chain ganglia in adult animals. We generated tissue blocks that contained specific components of the SNS of adult mice and subjected them to a modified iDISCO clearing protocol with immunohistochemistry for TH and other markers. This revealed for the first time in adult mice the undisturbed three-dimensional structure of the bilateral sympathetic chain and intercostal nerves, as well as adrenergic nerves and neurons in the neck and brain (Fig. 1E and Supplementary Video S1, online only). Specifically, using classical or light sheet confocal microscopy, the individual anatomy of the stellate to T13 and lumbar sympathetic chain ganglia and interconnecting nerve strands were revealed in their three-dimensional space on a background of rib and vertebral column structure, which did not completely clear.

### PRV mapping of iBAT-innervating neurons in sympathetic chain ganglia and spinal cord

PRV has been widely used to identify autonomic nervous system (ANS) innervation of peripheral tissues and is the retrograde tracer of choice.[32] We injected GFP-conjugated PRV unilaterally into the right iBAT pad. Our focus was on first- and second-order neurons only (pre- and postganglionic neurons), so that the survival time after virus injections was kept short with 3–4 days.

Labeling in the stellate ganglia and upper thoracic sympathetic chain ganglia on the ipsilateral injection side could be seen in fixed and eviscer-

ated whole animal preparations using a fluorescence stereomicroscope (Fig. 1C), which guided dissection as above. After iDISCO clearance with the immunohistochemical enhancement of viral GFP and TH, much more details became visible with classical and light sheet confocal microscopy (Figs. 2 and 3). Specifically, there was strong labeling not only in the caudal portion of the stellate ganglion, but also in the thoracic chain ganglia from T1 (typically fused to the stellate ganglion) to T5, and in some cases scattered labeling up to T7. Labeling was limited to the ipsilateral side of the injection, even though we observed rare cases of bilateral labeling, likely due to accidental injection into the adjacent and merged left iBAT section. Labeling in the T5 to T7 ganglia became increasingly sparse.

Higher magnification images clearly revealed individual PRV-infected neurons among noninfected TH-positive neurons (Fig. 3). In addition, PRV-labeled nerve fibers within intercostal nerves and ganglia connecting nerve strands could be discerned on the background of TH-positive nerves.

Importantly, injection of the same viral dose in mice with prior surgical iBAT denervation (Fig. 4A and B), or dribbling it over the surface of iBAT (data not shown), did not result in any discernible labeling in any sympathetic chain ganglia. TH labeling also revealed the location of the DRG as well as the paravertebral ganglia and we inspected these ganglia for PRV-labeled neurons. We found no indication of PRV labeling in paravertebral abdominal ganglia, such as the celiac (Fig. 4C) and splanchnic nerves, even though a few iBAT projecting DRG neurons were identified with PRV labeling (Fig. 4D–G).

Quantitative analysis of nine successful PRV injections revealed that about half of PRV-labeled neurons were located in the fused stellate/T1 ganglion and the other half was distributed over T2–T5 (Fig. 5 and Table S2, online only). However, the number of labeled neurons in the stellate/T1 ganglia varied widely, indicating either a biological variation or incomplete labeling.

To map the preganglionic neurons in the spinal cord that innervate iBAT, light sheet microscopy was performed on cleared tissue blocks from seven mice containing the spinal cord and the sympathetic chain (Fig. 6A). PRV labeling in the IML column of the spinal cord was found between rostrocaudal levels T2–T8 (Fig. 6B). None of these seven mice
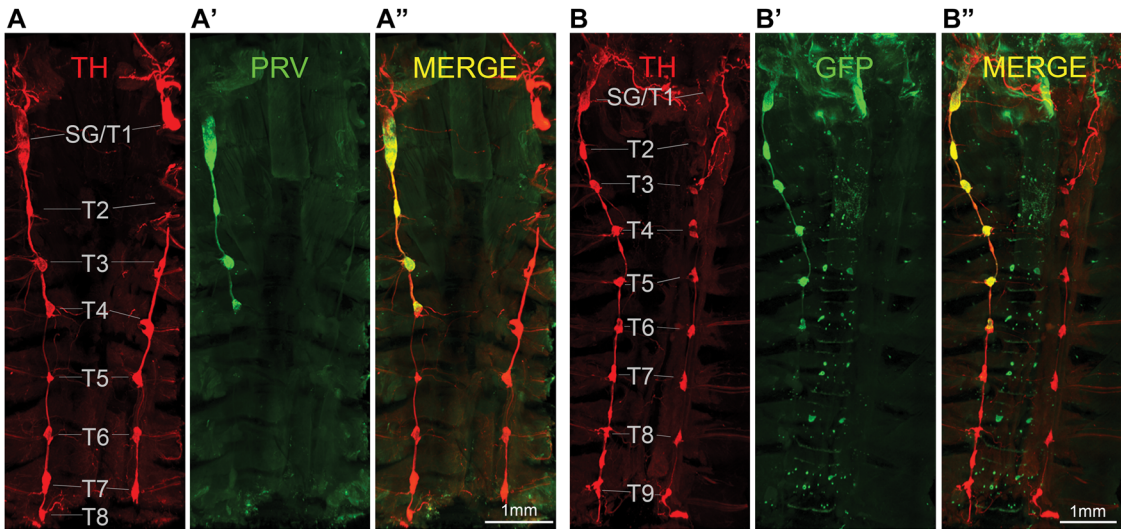
**Figure 2.** Ventral overview of sympathetic postganglionic ganglia innervating iBAT in the mouse as shown by two examples with unilateral PRV injections in the right iBAT pad (A and B). Confocal microscope images of tyrosine hydroxylase (TH) (A and B), PRV with GFP expression (PRV-GFP) (A' and B') and merged images (A" and B") from iDISCO-processed whole tissue blocks. Note retrograde labeling of the right stellate/T1 ganglion, as well as T2−T4 in example A and T2−T6 in example B.

showed preganglionic labeled neurons at the level of the stellate/T1 ganglia or beyond T9, all seven mice showed labeling at levels T2−T6, and labeling from T7 to T8 was found in a subset of animals. Thus, the representation of preganglionic neurons innervating iBAT is slightly shifted to more caudal levels as compared to the corresponding postganglionic neurons (Fig. 6C).

## Discussion and conclusions

Brown fat thermogenesis is an evolutionarily conserved mechanism to maintain body temperature in mammals and has the potential to convert surplus energy into heat for better energy balance control in an environment of plenty.[15,33] In addition, BAT may be the source of factors and hormones that play important roles in metabolic health.[30,34−36] Because sympathetic drive is required for optimal BAT function,[37,38] identification of the sympathetic pre- and postganglionic neurons selectively innervating BAT is important. Here, we combine classical pseudorabies retrograde tracing with transgenic mouse models, whole tissue clearing, and confocal light sheet microscopy to show the specific distribution of sympathetic postganglionic neurons innervating the iBAT in the mouse. We identified suitable reporter mice to guide initial dissection of large tissue blocks containing the critical

components, which greatly increases confidence in anatomical dissection and sectioning techniques. We further adapt iDSICO methods to immunohistochemically stain and perform tissue clearance of the entire spinal cord and sympathetic chain in the adult mouse. This approach is able to visualize the entire SNS and its major components undisturbed *in situ,* and greatly facilitates the unbiased and transparent evaluation of pre- and postganglionic contribution to iBAT innervation. Contrary to findings in the rat[39,40] and Siberian hamster,[41] we find iBAT-innervating sympathetic postganglionic neurons not just in the stellate ganglion but also in the T2−T5 sympathetic chain ganglia. Interestingly, within the stellate ganglion, the rostral pole is suspiciously void of neurons innervating iBAT. The rostral pole is known to harbor postganglionic neurons that innervate the heart.[42,43] In contrast, the more caudal portions of the stellate ganglia together with the T1, T2, T3, T4, and T5 chain ganglia are densely packed with iBAT-innervating neurons. Future studies will further investigate how the sympathetic nerves leaving these individual ganglia relate to the organization of end-organ iBAT innervation.

Importantly, we did not find any iBAT-innervating postganglionic neurons in the lower sympathetic chain ganglia as reported for the
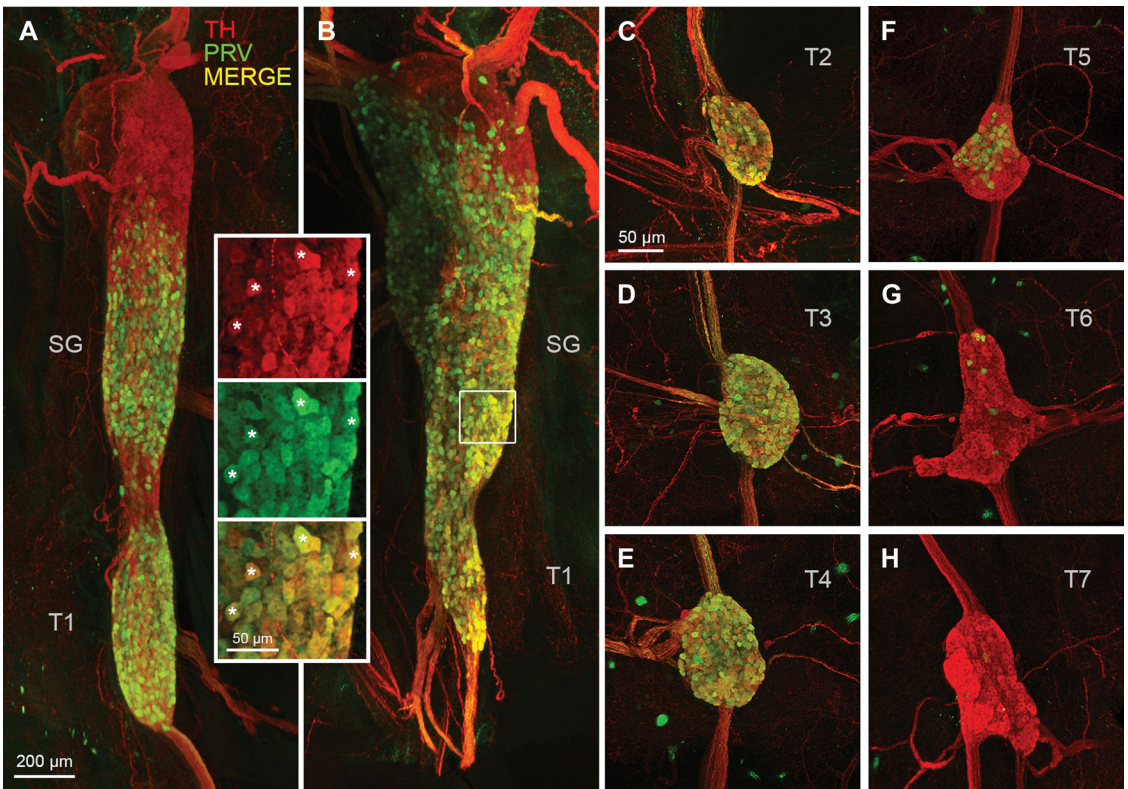
**Figure 3.** Postganglionic sympathetic neurons innervating iBAT in the mouse. (A and B) Light sheet microscope images of two examples of retrogradely PRV-labeled postganglionic sympathetic neurons in the fused right stellate/T1 ganglion after unilateral PRV injections into the right iBAT pad. Inset shows retrogradely PRV-labeled (green) and unlabeled (red) neurons at higher magnification (asterisks depict examples of colocalized neurons). (C–H) Confocal microscope images of individual sympathetic chain ganglia at thoracic levels T2−T7 in the same mouse for which the stellate ganglion is shown in (B). Note strong labeling in T2−T4 and much weaker labeling in T5 and T6 ganglia. TH, tyrosine hydroxylase; PRV, pseudorabies virus; SG, stellate ganglion; T1−T7, ganglia for thoracic levels 1−7.

Siberian hamster.[44] This is consistent with the overall development of sympathetic innervation that clearly dissociates the origin of sympathetic innervation in anterior (thorax and forelimbs), posterior (hind limb), and abdominal (*situ*) sites,[45] and classic views of autonomic innervation.[39] A few PRV-labeled neurons were found in DRG, and it is not clear whether these are true sympathetic efferent neurons or inadvertently anterograde labeled dorsal root afferents. Given the very small number of these neurons, they are not likely to be of major physiological importance.

Our analysis of preganglionic neurons in the spinal cord is in general agreement with studies in the rat[39,46] and Siberian hamster,[44] which all report the stellate ganglion as a major contribution to the sympathetic innervation of the iBAT. How-

ever, our data highlight the regional distribution of PRV labeling within the stellate ganglion and the lack of PRV labeling in the dorsal pole. Furthermore, we clarify that thoracic ganglia from the stellate until T5 significantly contribute to iBAT innervation, with scattered PRV labeling in T6/T7 and no contribution was observed below T8 chain ganglia, contrary to a report by Nguyen *et al.*[44] We also clarified that the prevertebral celiac ganglion did not innervate iBAT, which has been recently suggested as the main innervation site of adipose tissue.[47] Our study is also the first to investigate systematically the anatomical extent of preganglionic iBAT innervating neurons in the IML (levels T2–T6).

Our study demonstrates the usefulness and points out some caveats of genetically altered mouse models for the analysis of ANS functional anatomy
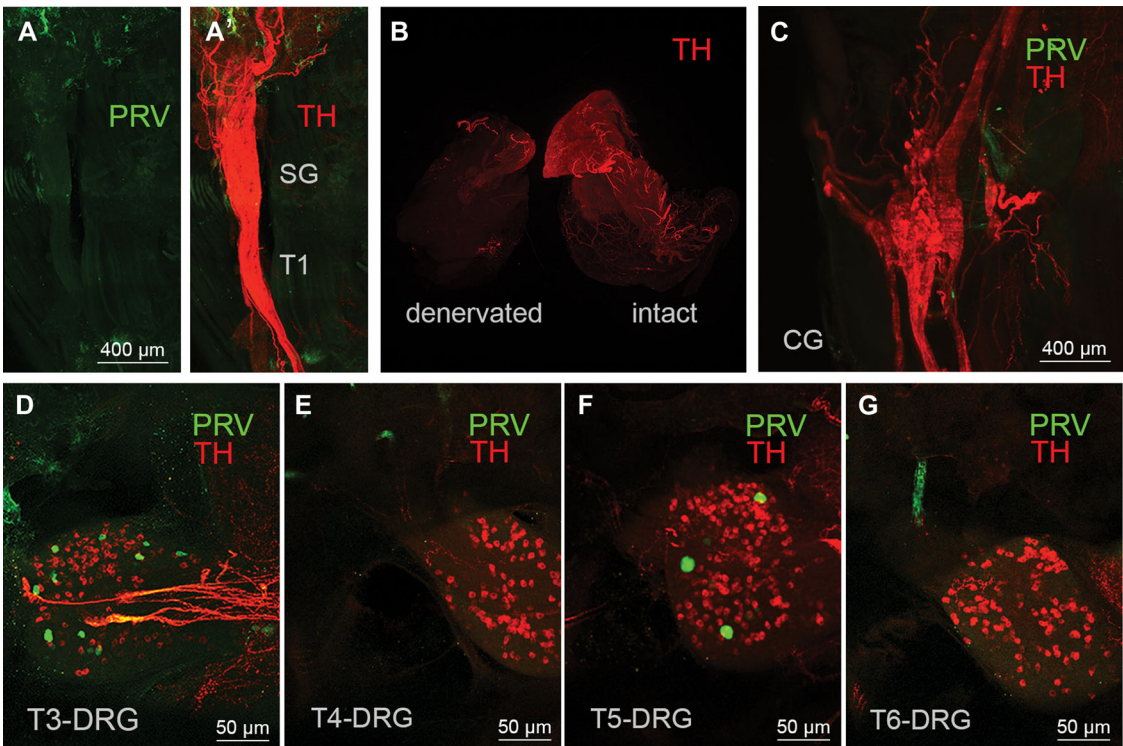
**Figure 4.** Controls for nonspecific labeling. (A and B) Light sheet microscope images of the fused right stellate/T1 ganglion showing the absence of PRV-labeled neurons (green) in mouse with PRV injections into surgically denervated right iBAT pad. (A') Same ganglion with TH fluorescence (red) to show the outline of the ganglion. The sympathetic innervation (TH labeling) is degraded in the denervated iBAT pad, in contrast to the intact iBAT pad (B). (C) Light sheet microscope image of a mouse with successful PRV labeling in sympathetic chain ganglia shows a complete absence of PRV labeling in the celiac ganglion (CG). (D–G) Confocal microscope images of a mouse with successful PRV labeling in sympathetic chain ganglia show sparse PRV labeling (green dots) in T3-DRG (D), T4-DRG (E), T5-DRG (F), and T6-DRG (G). TH, tyrosine hydroxylase; PRV, pseudorabies virus; SG, stellate ganglion; DRG, dorsal root ganglion; T1–T7, ganglia for thoracic levels 1–7.
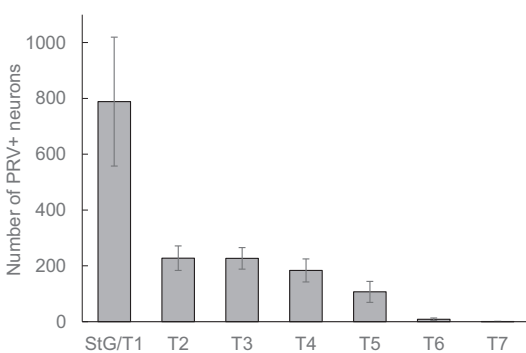


**Figure 5.** Quantitative distribution of sympathetic postganglionic neurons innervating iBAT in the mouse. Mean ± SEM of number of retrogradely labeled neurons in mice ($n = 9$) unilaterally injected with PRV into the left iBAT pad. Note that about half the retrogradely labeled neurons are located in the fused stellate/T1 ganglion and the other half is distributed over T1–T5 ganglia.

that should be very helpful for other studies. The TH-IRES-Cre knock-in and the transgenic Dbh-Cre mice were both useful reporter driver in the SNS, while the transgenic TH-Cre mouse resulted only in sporadic cell bodies with reporter expression throughout the thoracic chain ganglia, which requires consideration when choosing Cre-driver lines for studies in peripheral sympathetic nerves. However, with appropriate Cre-driver lines, the red fluorescent signal in the reporter mice was strong enough to guide dissection of any component of the SNS in fresh or formalin perfused preparations under a fluorescent stereomicroscope. Other methods that have been used in the past are IP injections of Fluoro-Gold[TM],[48] which label all neurons of the peripheral nervous system (sympathetic, parasympathetic, and sensory) in rats and mice,[48,49] but genetic approaches hold promise for a better
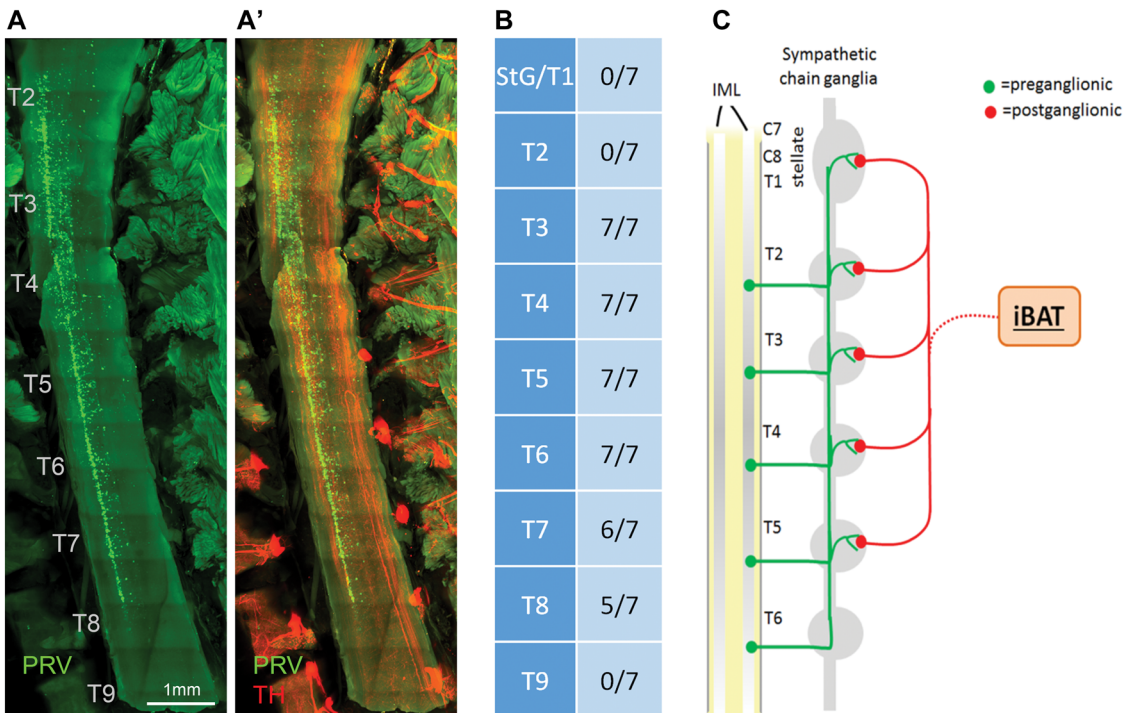
**Figure 6.** Location of sympathetic preganglionic neurons innervating iBAT and schematic diagram of sympathetic outflow pattern to iBAT in the mouse. (A and A') Light sheet microscope image through spinal cord showing the location of preganglionic neurons (green) on the right side of the intermediolateral column (A), and merged image of PRV and TH (A') in a mouse with unilateral injection of PRV into the left iBAT pad. (B) Semiquantitative assessment of location of postganglionic neurons in the spinal cord relative to the rostrocaudal level. Note the caudal-ward shift in representation with no preganglionic neurons at the level of the fused stellate/T1, T2, and T9 sympathetic chain ganglion. (C) Schematic diagram depicting the organization of sympathetic outflow to iBAT in the mouse. IML, intermediolateral column of the spinal cord.

distinction of sympathetic, parasympathetic, sensory, and enteric nervous system components and do not require dissection under harmful UV light.

Our study also highlights that immunohistochemical staining and tissue clearance protocols are successful in adult animals with excellent resolution for the peripheral nervous system and greatly enhance the rigor and transparency of analyzed anatomical levels. With the ascent of neural modulation devices and therapies,[50–53] it will be important to provide detailed, complete, and specific functional maps of peripheral nervous systems. To this end, analysis of large tissue blocks allowing complete spatial representation of all nerves and ganglia vis-à-vis specific target organs will be indispensable. The methodology described here should enable high-resolution 3D imaging of sympathetic and parasympathetic innervation of other important target organs, such as white adipose tissue, gut, pancreas, liver, kidneys, spleen, the urogenital tract, and the respiratory system.

One potential limitation of using mice and other small mammals as models to gain basic information on the functional anatomy of the ANS is the possibility of significant differences to humans. Specifically, comparisons of SNS innervation of BAT between rodents and humans are complicated by the fact that in humans it appears to be located and distributed quite differently than in rodents. Instead of the prominent iBAT pad in rodents, the most important accumulation of BAT in humans is supraclavicular, with additional depots in the neck and along the spinal cord vertebrae.[3,4] Even though the different distribution will likely not affect the functional importance of BAT per se, future studies in mice to modulate sympathetic iBAT function are important approaches to understanding metabolic dynamics in humans.

In conclusion, using transgenic TH-IRES-Cre mice, whole tissue clearing, and confocal/light sheet microscopy, we provide a complete map of SNS innervation of the mouse iBAT depot that shows the location of postganglionic sympathetic neurons not confined to the stellate ganglia, but also the first several sympathetic chain ganglia.

## Acknowledgment

## Supporting information

Additional supporting information may be found in the online version of this article.

**Table S1**. Detailed information on mouse models, pseudorabies virus, and antibody used.

**Table S2**. Individual data for automated cell counts of PRV-GFP–labeled neurons in sympathetic chain ganglia using IMARIS software.

**Supplementary Video S1**. 3D confocal image of an iDISCO cleared thorax showing sympathetic neurons (tyrosin hydroxylase (TH), red) and pseudorabies virus retrogradely labeled from the right interscapular brown adipose tissue (PRV-GFP, green).

## Competing interests

The authors declare no competing interests.

## References

1. Huttunen, P., J. Hirvonen & V. Kinnula. 1981. The occurrence of brown adipose tissue in outdoor workers. *Eur. J. Appl. Physiol. Occup. Physiol.* **46:** 339–345.
2. Rothwell, N.J. & M.J. Stock. 1979. A role for brown adipose tissue in diet-induced thermogenesis. *Nature* **281:** 31–35.
3. Cohade, C., M. Osman, H.K. Pannu, *et al.* 2003. Uptake in supraclavicular area fat ("USA-Fat"): description on 18F-FDG PET/CT. *J. Nucl. Med.* **44:** 170–176.
4. Saito, M., Y. Okamatsu-Ogura, M. Matsushita, *et al.* 2009. High incidence of metabolically active brown adipose tissue in healthy adult humans: effects of cold exposure and adiposity. *Diabetes* **58:** 1526–1531.
5. Nedergaard, J., T. Bengtsson & B. Cannon. 2007. Unexpected evidence for active brown adipose tissue in adult humans. *Am. J. Physiol. Endocrinol. Metab.* **293:** E444–E452.
6. Cypess, A.M., S. Lehman, G. Williams, *et al.* 2009. Identification and importance of brown adipose tissue in adult humans. *N. Engl. J. Med.* **360:** 1509–1517.
7. Virtanen, K.A., M.E. Lidell, J. Orava, *et al.* 2009. Functional brown adipose tissue in healthy adults. *N. Engl. J. Med.* **360:** 1518–1525.
8. van Marken Lichtenbelt, W.D., J.W. Vanhommerig, N.M. Smulders, *et al.* 2009. Cold-activated brown adipose tissue in healthy men. *N. Engl. J. Med.* **360:** 1500–1508.
9. Lee, P., M.M. Swarbrick & K.K. Ho. 2013. Brown adipose tissue in adult humans: a metabolic renaissance. *Endocr. Rev.* **34:** 413–438.
10. Virtanen, K.A., W.D. van Marken Lichtenbelt & P. Nuutila. 2013. Brown adipose tissue functions in humans. *Biochim. Biophys. Acta* **1831:** 1004–1008.
11. Au-Yong, I.T., N. Thorn, R. Ganatra, *et al.* 2009. Brown adipose tissue and seasonal variation in humans. *Diabetes* **58:** 2583–2587.
12. Chen, K.Y., R.J. Brychta, J.D. Linderman, *et al.* 2013. Brown fat activation mediates cold-induced thermogenesis in adult humans in response to a mild decrease in ambient temperature. *J. Clin. Endocrinol. Metab.* **98:** E1218–E1223.
13. Cohade, C., K.A. Mourtzikos & R.L. Wahl. 2003. "USA-fat": prevalence is related to ambient outdoor temperature-evaluation with 18F-FDG PET/CT. *J. Nucl. Med.* **44:** 1267–1270.
14. Vosselman, M.J., B. Brans, A.A. van der Lans, *et al.* 2013. Brown adipose tissue activity after a high-calorie meal in humans. *Am. J. Clin. Nutr.* **98:** 57–64.
15. Rothwell, N.J. & M.J. Stock. 1983. Luxuskonsumption, diet-induced thermogenesis and brown fat: the case in favour. *Clin. Sci. (Lond.)* **64:** 19–23.
16. Giordano, A., A. Frontini, M. Castellucci, *et al.* 2004. Presence and distribution of cholinergic nerves in rat mediastinal brown adipose tissue. *J. Histochem. Cytochem.* **52:** 923–930.
17. Lidell, M.E., M.J. Betz, O. Dahlqvist Leinhard, *et al.* 2013. Evidence for two types of brown adipose tissue in humans. *Nat. Med.* **19:** 631–634.
18. Cypess, A.M., A.P. White, C. Vernochet, *et al.* 2013. Anatomical localization, gene expression profiling and functional characterization of adult human neck brown fat. *Nat. Med.* **19:** 635–639.
19. Andrews, P.L., N.J. Rothwell & M.J. Stock. 1985. Influence of subdiaphragmatic vagotomy and brown fat sympathectomy on thermogenesis in rats. *Am. J. Physiol.* **249:** E239–E243.
20. Bartness, T.J. & G.N. Wade. 1984. Effects of interscapular brown adipose tissue denervation on body weight and energy metabolism in ovariectomized and estradiol-treated rats. *Behav. Neurosci.* **98:** 674–685.
21. Festuccia, W.T., P.G. Blanchard, D. Richard, *et al.* 2010. Basal adrenergic tone is required for maximal stimulation of rat brown adipose tissue UCP1 expression by chronic PPAR-gamma activation. *Am. J. Physiol. Regul. Integr. Comp. Physiol.* **299:** R159–R167.
22. Geloen, A., A.J. Collet & L.J. Bukowiecki. 1992. Role of sympathetic innervation in brown adipocyte proliferation. *Am. J. Physiol.* **263:** R1176–R1181.
23. Granneman, J.G. & R.G. Campbell. 1984. Effects of sucrose feeding and denervation on lipogenesis in brown adipose tissue. *Metabolism* **33:** 257–261.
24. Himms-Hagen, J., J. Cui & S. Lynn Sigurdson. 1990. Sympathetic and sensory nerves in control of growth of brown adipose tissue: effects of denervation and of capsaicin. *Neurochem. Int.* **17:** 271–279.

25. Pulinilkunnil, T., H. He, D. Kong, *et al.* 2011. Adrenergic regulation of AMP-activated protein kinase in brown adipose tissue *in vivo*. *J. Biol. Chem.* **286:** 8798–8809.

26. Takahashi, A., T. Shimazu & Y. Maruyama. 1992. Importance of sympathetic nerves for the stimulatory effect of cold exposure on glucose utilization in brown adipose tissue. *Jpn. J. Physiol.* **42:** 653–664.

27. Tsukazaki, K., H. Nikami, Y. Shimizu, *et al.* 1995. Chronic administration of beta-adrenergic agonists can mimic the stimulative effect of cold exposure on protein synthesis in rat brown adipose tissue. *J. Biochem.* **117:** 96–100.

28. Iwami, M., F. Alkayed, T. Shiina, *et al.* 2013. Activation of brown adipose tissue thermogenesis by electrical stimulation to the dorsal surface of the tissue in rats. *Biomed. Res.* **34:** 173–178.

29. Bartness, T.J., Y.B. Shrestha, C.H. Vaughan, *et al.* 2010. Sensory and sympathetic nervous system control of white adipose tissue lipolysis. *Mol. Cell. Endocrinol.* **318:** 34–43.

30. Zhang, Y., I.A. Kerman, A. Laque, *et al.* 2011. Leptin-receptor-expressing neurons in the dorsomedial hypothalamus and median preoptic area regulate sympathetic brown adipose tissue circuits. *J. Neurosci.* **31:** 1873–1884.

31. Renier, N., Z. Wu, D.J. Simon, *et al.* 2014. iDISCO: a simple, rapid method to immunolabel large tissue samples for volume imaging. *Cell* **159:** 896–910.

32. Card, J.P. & L.W. Enquist. 2014. Transneuronal circuit analysis with pseudorabies viruses. *Curr. Protoc. Neurosci.* **68:** 1.5.1–1.5.39.

33. Cannon, B. & J. Nedergaard. 2010. Metabolic consequences of the presence or absence of the thermogenic capacity of brown adipose tissue in mice (and probably in humans). *Int. J. Obes. (Lond.)* **34**(Suppl. 1): S7–S16.

34. Nedergaard, J., T. Bengtsson & B. Cannon. 2011. New powers of brown fat: fighting the metabolic syndrome. *Cell Metab.* **13:** 238–240.

35. Cypess, A.M., C.R. Haft, M.R. Laughlin, *et al.* 2014. Brown fat in humans: consensus points and experimental guidelines. *Cell Metab.* **20:** 408–415.

36. Kong, X., T. Yao, P. Zhou, *et al.* 2018. Brown adipose tissue controls skeletal muscle function via the secretion of myostatin. *Cell Metab.* **28:** 631–643.e3.

37. Dulloo, A.G. & D.S. Miller. 1984. Energy balance following sympathetic denervation of brown adipose tissue. *Can. J. Physiol. Pharmacol.* **62:** 235–240.

38. Denjean, F., J. Lachuer, A. Geloen, *et al.* 1999. Differential regulation of uncoupling protein-1, -2 and -3 gene expression by sympathetic innervation in brown adipose tissue of thermoneutral or cold-exposed rats. *FEBS Lett.* **444:** 181–185.

39. Wiedmann, N.M., A. Stefanidis & B.J. Oldfield. 2017. Characterization of the central neural projections to brown, white, and beige adipose tissue. *FASEB J.* **31:** 4879–4890.

40. Stefanidis, A., N.M. Wiedmann, S. Tyagi, *et al.* 2018. Insights into the neurochemical signature of the Innervation of Beige Fat. *Mol. Metab.* **11:** 47–58.

41. Bamshad, M., C.K. Song & T.J. Bartness. 1999. CNS origins of the sympathetic nervous system outflow to brown adipose tissue. *Am. J. Physiol.* **276:** R1569–R1578.

42. Hopkins, D.A. & J.A. Armour. 1984. Localization of sympathetic postganglionic and parasympathetic preganglionic neurons which innervate different regions of the dog heart. *J. Comp. Neurol.* **229:** 186–198.

43. Buckley, U., K. Yamakawa, T. Takamiya, *et al.* 2016. Targeted stellate decentralization: implications for sympathetic control of ventricular electrophysiology. *Heart Rhythm* **13:** 282–288.

44. Nguyen, N.L., C.L. Barr, V. Ryu, *et al.* 2017. Separate and shared sympathetic outflow to white and brown fat coordinately regulates thermoregulation and beige adipocyte recruitment. *Am. J. Physiol. Regul. Integr. Comp. Physiol.* **312:** R132–R145.

45. Glebova, N.O. & D.D. Ginty. 2005. Growth and survival signals controlling sympathetic nervous system development. *Annu. Rev. Neurosci.* **28:** 191–222.

46. Nakamura, K., K. Matsumura, T. Hubschle, *et al.* 2004. Identification of sympathetic premotor neurons in medullary raphe regions mediating fever and other thermoregulatory functions. *J. Neurosci.* **24:** 5370–5380.

47. Jiang, H., X. Ding, Y. Cao, *et al.* 2017. Dense intra-adipose sympathetic arborizations are essential for cold-induced beiging of mouse white adipose tissue. *Cell Metab.* **26:** 686–692.e3.

48. Powley, T.L. & H.R. Berthoud. 1991. A fluorescent labeling strategy for staining the enteric nervous system. *J. Neurosci. Methods* **36:** 9–15.

49. Berthoud, H.R. & T.L. Powley. 1996. Interaction between parasympathetic and sympathetic nerves in prevertebral ganglia: morphological evidence for vagal efferent innervation of ganglion cells in the rat. *Microsc. Res. Tech.* **35:** 80–86.

50. Lee, S. & A. Abd-Elsayed. 2016. Some non-FDA approved uses for neuromodulation in treating autonomic nervous system disorders: a discussion of the preliminary support. *Neuromodulation* **19:** 791–803.

51. Gofeld, M. 2014. New horizons in neuromodulation. *Curr. Pain Headache Rep.* **18:** 397.

52. Guiraud, D., D. Andreu, S. Bonnet, *et al.* 2016. Vagus nerve stimulation: state of the art of stimulation and recording strategies to address autonomic function neuromodulation. *J. Neural Eng.* **13:** 041002.

53. Hou, Y., Q. Zhou & S.S. Po. 2016. Neuromodulation for cardiac arrhythmia. *Heart Rhythm* **13:** 584–592.